CrossMark

Analysis of Oxides Formed on the Surface of the Alloy 690 in Hydrogenated Supercritical Water

Jin Gao[1] · Fa-rong Wan[1] · Guo-ping Cao[2] · Kumar Sridharan[2] · Todd Allen[2]

Abstract The oxides formed on the surface of the alloy 690 in hydrogenated supercritical water at 400 °C for 1000 h were investigated using scanning electron microscopy, transmission electron microscopy, scanning transmission electron microscopy and energy-dispersive X-ray spectroscopy. The oxides on the surface of the alloy 690 exhibited multi-layer structure: an outer layer consisted of granular crystallites (NiO and $NiFe_2O_4$) and a compact inner layer (spinel and Cr_2O_3). Chemical analysis indicated that the outer layer was enriched in nickel but depleted in chromium, whereas the inner layer was enriched in chromium and iron but depleted in nickel. The inner layer was also characterized as layered structure by Fe-rich spinel on top of continuous Cr_2O_3 layer. Besides, Cr_2O_3 nodules were readily observed at the oxides/alloy interface.

KEY WORDS: Alloy 690; Supercritical water; Oxides; Corrosion

1 Introduction

Alloy 600 has been used extensively in nuclear power plants, but many failures have occurred after long-term operation. There are a number of researches on the susceptibility of the nickel alloys to the stress corrosion cracking (SCC) to be reported [1–5]. Hydrogen is often added to high temperature water to maintain low level of dissolved oxygen. In particular, the effect of the dissolved hydrogen (DH) on alloy 600 in pressurized water reactors (PWRs) has been paid much attention in recent years [6–9]. Nakagawa et al. [10] studied the influence of dissolved hydrogen on oxide film of alloy 600 in PWR primary water at 320 °C with content of dissolved hydrogen from 0 to 45 cc/kg H_2O. According to the oxide film analysis, the oxide films formed below 11 cc/kg H_2O of dissolved hydrogen were relatively thick and rich in Ni, but those formed at higher dissolved hydrogen content were relatively thin and rich in Cr and Fe. Terachi et al. [11] studied the changes in the oxide films that formed on alloy 600 with an increase in DH content (0–4.0 mg/L) in PWR primary water at 320 °C. Their results indicated that multi-layer oxide films, including a Cr-rich inner layer and NiO or (Ni, Cr, Fe) spinel oxide outer layers on the surface of the alloy 600 were formed, and the structure of each layer changed with DH content. Attanasio and Morton [12] reported that the maximum primary water SCC susceptibility in alloy 600 occurred at proximity to nickel/nickel oxide (Ni/NiO) phase transition. Based on this criterion, the dissolved hydrogen in our study was controlled around Ni/NiO corrosion boundary.

Alloy 690 with nominal composition (Ni—10% Fe— 30% Cr) as an alternative for alloy 600 has been increasingly used for steam generator tubing in PWRs due to its superior SCC resistance. However, the failures of the

✉ Fa-rong Wan
  wanfr@mater.ustb.edu.cn

1 School of Materials Science and Engineering, University of Science and Technology Beijing, Beijing 100083, China

2 Department of Materials Science and Engineering, University of Wisconsin-Madison, Madison, WI 53706, USA

components made of the alloy 690 have rarely been reported. Therefore, the long-term corrosion performance of the alloy has been concerned highly. Some laboratory experiments revealed that this kind of the alloys were not immune to SCC in primary water [5, 13, 14], as well as in caustic solutions [15]. Kim et al. [16] reported that alloy 690 was very susceptible to SCC in a strong alkaline solution where the oxide is not stable and solubility is high. The composition and structure of the oxide formed on the surface of the alloy determine the protection ability of the oxide and thus play a crucial role in the corrosion behavior. However, a couple of factors, including chemical composition of the alloy, alloy treatments [13, 17–19], water chemistry [20–23] and surface finishing condition [24, 25], influence the oxide film characteristic in terms of oxide morphology, structure and chemical composition. According to Huang et al. [23], the change in water chemistry from pure to primary water was found to vary the film structure from duplex layer, including an outer layer of granular Fe-rich spinel and NiO, and a porous inner layer mainly composing of nickel oxides, to triple layer with an intermediate layer of filamentous NiO. Zhong et al. [26] studied the corrosion behavior of alloy 690 in aerated supercritical water (SCW). A duplex oxide layer structure including a Cr-rich compact inner layer grown via solid-state growth mechanism and Ni-rich porous outer layer grown via metal dissolution/oxide precipitation mechanism was formed. Similar results obtained by Kuang et al. [27] showed that Cr-rich oxides formed initially through solid-state reactions and Ni–Fe spinels gradually developed on the surface layer by precipitation with increasing immersion time exposed to 290 °C water containing 3 ppm O_2. It was found that Cr was preferentially oxidized and tended to dissolve into solution. As a result, the inner layer was mainly consisted of NiO, which could not serve as a protective barrier layer. With respect to the effect of surface roughness on corrosion resistance, it has been shown that corrosion rate decreased with a decrease in roughness value [24, 25].

Supercritical water (SCW) has been used as a simulated testing system for the primary water reactor environment. A better understanding of the nature and structure of oxides formed on alloy 690 helps us to better understand the mechanism of SCC in nickel-based alloys. This paper focused on the analysis of oxides formed on the surface of the alloy 690 exposed to hydrogenated SCW.

2 Experimental

The sample used in this study was mill annealed alloy 690. Its chemical composition in weight percentage was shown in Table 1. Alloy 690 coupons of 15.88 mm × 12.60 mm × 1.02 mm in size were cut by electron discharge machine (EDM). All the samples were ground progressively with SiC emery paper to a grit of 2000 followed by electro-polishing.

The samples of alloy 690 were mounted to an Inconel 625 sample holder and then placed in the high temperature (400 °C)/high pressure (25 MPa) autoclave up to 1000 h. The dissolved hydrogen in this study was 107 cc/kg near the Ni/NiO corrosion boundary at NiO stable side.

Surface morphology was analyzed using FIB Zeiss 1500XB system working at 30 kV. The structures of the cross-section were observed using transmission electron microscopy (TEM). Cross-sectional samples were made using the same system with platinum on top surface as protection layer. A Titan scanning transmission electron microscope (STEM) with probe aberration corrector operated at 200 kV equipped with a high-angle angular-dark-field (HAADF) detector and energy-dispersive X-ray spectrum (EDS) system was used for imaging and compositional analysis. Selected-area diffraction was used to characterize the oxides.

## 3 Results

3.1 Surface Morphology

Weight changes of the samples were measured after the corrosion tests and all samples exhibited a positive weight gain, indicating that the oxides formed on top of the sample surface. As shown in Fig. 1, two different oxide particles, including large polyhedral crystallites and the small granular oxides, were observed. They showed cuboid crystallites (Fig. 1b) and triangular platelets (Fig. 1c) in shapes.

3.2 Oxide Structure

Figure 2 shows cross-sectional STEM HAADF images of alloy 690 exposed to hydrogenated SCW at 400 °C for 1000 h. The inset images on the upper row taken at high magnification indicated clearly the double-layer structures of the oxide: an outer layer and an inner fine-grain layer. For the outer layer, it is mainly composed of granular crystallites. Two families of crystallites can be distinguished according to their sizes: the "large ones" with a size larger than 500 nm and the "regular ones" with a size in the range of less than 100 nm, which is consistent with the observation shown in Fig. 1 by scanning electron microscopy (SEM). According to the results shown later, the "large ones" were spinel ferrites ($NiFe_2O_4$) and the "regular ones" were nickel oxides (NiO). As for the inner layer, it is a thin layer of fine-grain oxides. The thickness of

Table 1 Chemical composition of alloy 690 used in this study (wt%)

Alloy	Fe	Cr	Ni	C	Mn	Si	Mo	Cu	Other
Alloy 690	10	29.4	Bal.	0.03	0.18	0.03	–	0.01	S:0.001, Ti:0.34
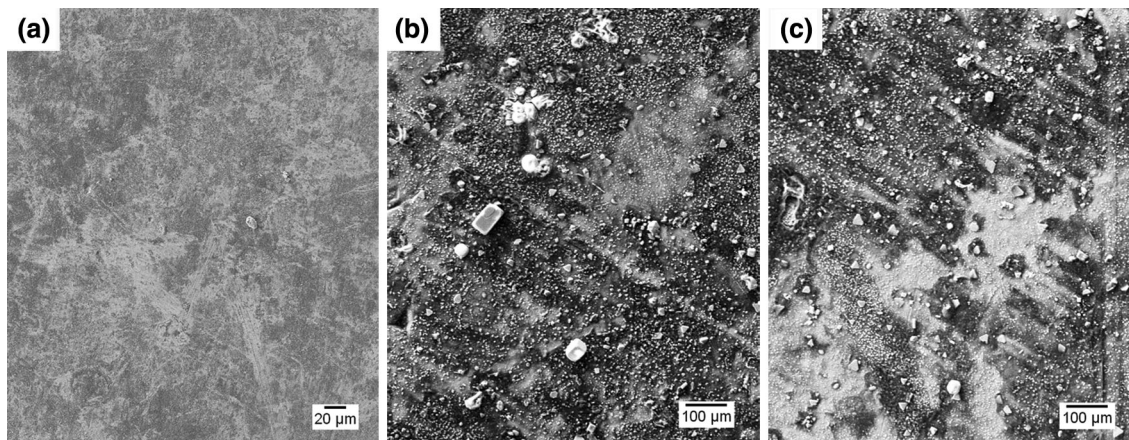
Fig. 1 Oxide images on the surface of alloy 690 exposed to hydrogenated SCW at 400 °C for 1000 h
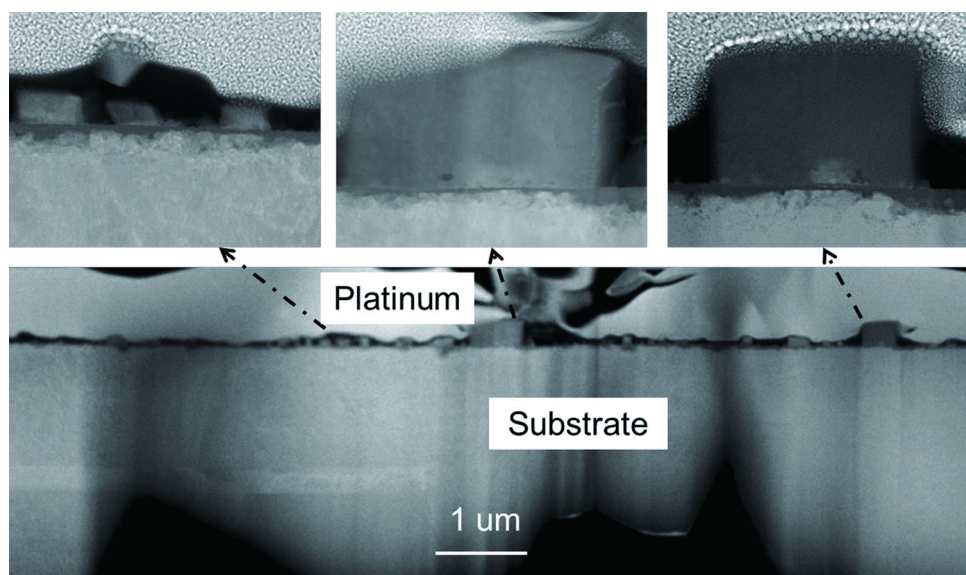
Fig. 2 STEM HAADF images of oxides on alloy 690 exposed to hydrogenated SCW at 400 °C for 1000 h

this layer varied along the surface, with some areas oxidized more deeply.

Figure 3a shows the STEM HAADF image of the outer granular crystallites. Figure 3b, d shows the high-resolution TEM images for the outer large crystallite and the inner layer between substrate and oxide, respectively. The large crystallite was characterized as nickel ferrite ($NiFe_2O_4$) which agrees with EDX results. EDX was performed at the large crystallite, and the results were shown in Table 2. The atomic ratio of Ni:Fe:O was around 1:2:4 and coincident with the HRTEM result. Oxide Cr_2O_3 was detected in the inner layer. Figure 3c shows the corresponding fast Fourier transformation (FFT) of HRTEM image (d), which highlights the presence of both $NiFe_2O_4$ and Cr_2O_3. It should be noted here that the HRTEM in Fig. 3b exhibited different patterns due to variation of the sample thickness from top to the bottom.
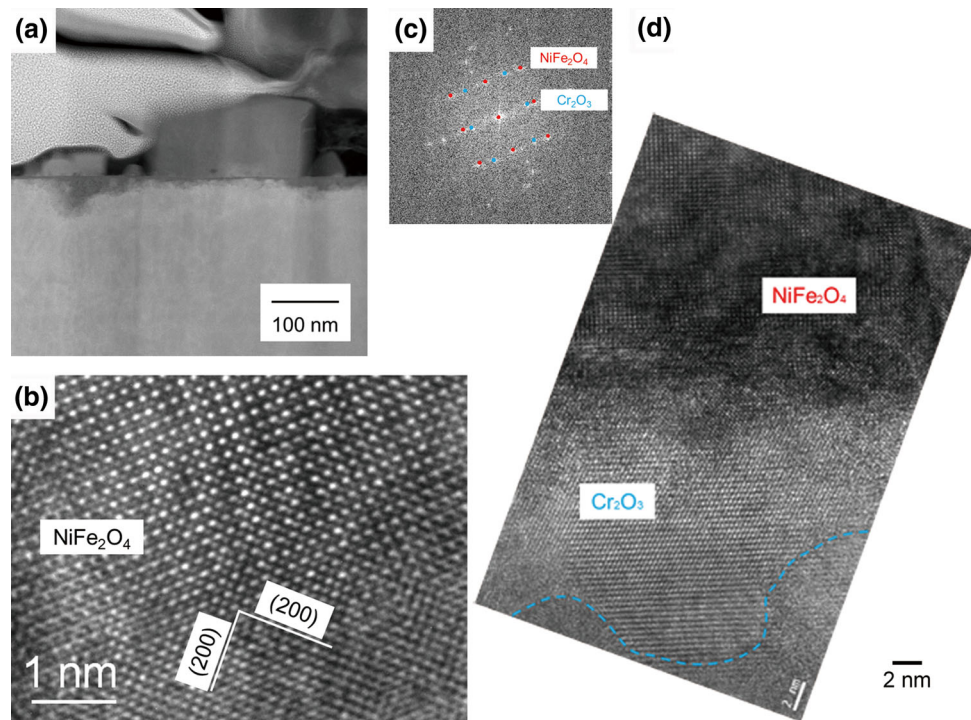
J. Gao *et al.*: Acta Metall. Sin. (Engl. Lett.), 2016, **29**(8), 774–781

777

Fig. 3 Oxides formed on the surface of the alloy 690 exposed to hydrogenated SCW at 400 °C for 1000 h: **a** STEM HAADF image; **b** high-resolution transmission electron microscopy (HRTEM) image for the large crystallite; **c** corresponding FFT of HRTEM image; **d** HRTEM image for both the inner and outer layers

Table 2 EDX results of the large outer oxide

Element	Weight (%)	Atomic (%)	Uncertainty (%)
O(K)	27.65	57.51	0.14
Cr(K)	0.44	0.28	0.99
Fe(K)	49.89	29.72	0.15
Ni(K)	22.00	12.47	0.11

Figure 4 highlights the internal oxidation and the variation of the thickness of the inner layer along the surface. Figure 4b, d are high-magnification images of Fig. 4a, c, respectively. It was revealed that the corrosion does not stop development at the oxide/alloy interface, but easily progresses into the substrate. Networks of Cr_2O_3 nodules with a size in the range of several nanometers were observed both in the inner layer and the substrate. Contrast of Cr_2O_3 can be easily recognized from the STEM HADDF image in Fig. 4b. Meanwhile, a Cr_2O_3-free layer was revealed on top of the underneath Cr_2O_3 layer. The thickness of the inner layer could reach a maximum depth around 100 nm under the $NiFe_2O_4$-free region, while this value decreased to 15 nm under the $NiFe_2O_4$ crystallite. Chromium-rich spinel containing both Ni and Fe was observed in the thick region, which was evidenced by selected-area diffraction patterns (SADPs) shown in Fig. 5.

3.3 Chemical Analysis

Figure 6 shows STEM image and corresponding EDX mapping of the oxides formed on the surface of the alloy 690 after 1000 h duration in hydrogenated SCW. From the oxygen map, it clearly highlights the internal oxidation in the substrate. The bright region under the inner layer was enriched in nickel containing iron and chromium but depleted in oxygen, indicating that the alloy was not oxidized. Compared with chromium and nickel maps, it was clearly demonstrated that the out layer was depleted in chromium, while the inner layer was depleted in nickel. For the iron, it was a little enriched in the intermediate layer between the outmost and the innermost layer.

Figure 7a shows STEM images indicating the compact oxide layer and the substrate below across a grain boundary and the EDX mapping. The gray phase along the grain boundaries was identified to be chromium carbide. According to the EDX mapping, the inner layer was also characterized as layered structure. Two distinct layers were detected with a Fe-rich oxide layer containing Ni on top of a continuous chromium-dominated oxide layer. Besides, oxidation along the grain boundary was not observed. Figure 7b shows STEM image and corresponding EDX profile of the thick inner oxide layer under the same experimental conditions. For the outmost small oxide, it is
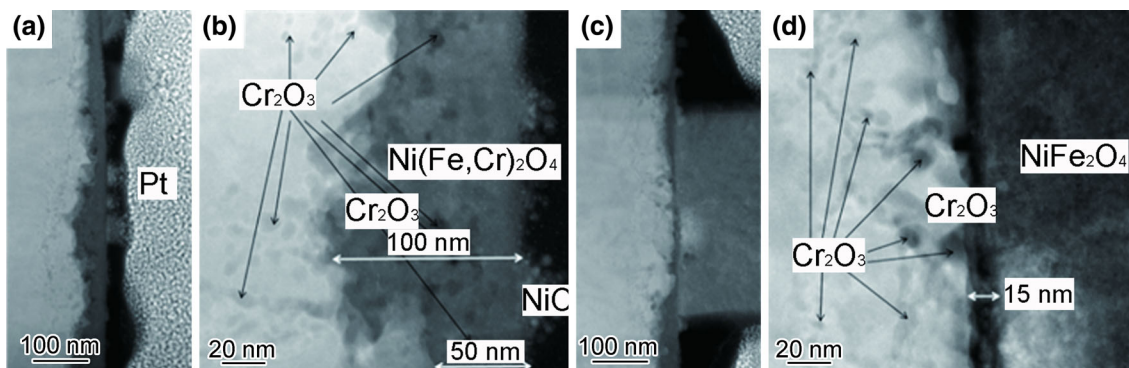
Fig. 4 High-magnification images for the oxide/alloy interface region of alloy 690 exposed to hydrogenated SCW at 400 °C for 1000 h: **a** and **b** for the thick inner layer under the small NiO; **c** and **d** for the thin layer under the large $NiFe_2O_4$
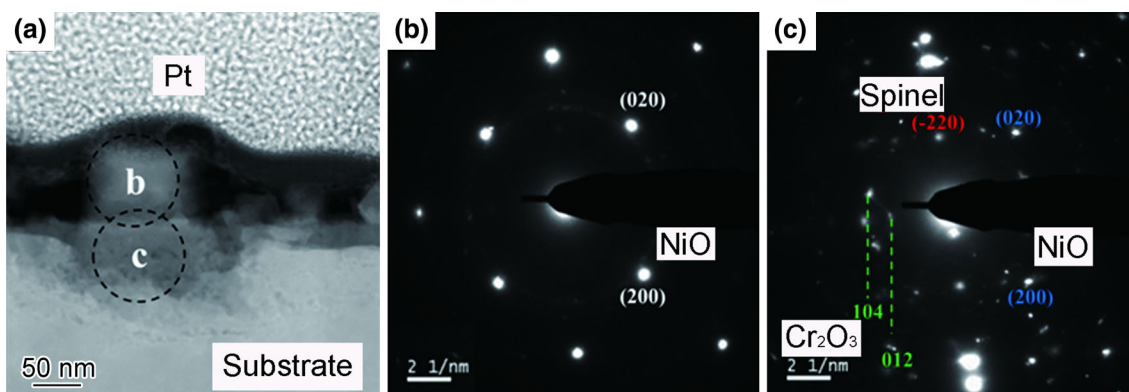

Fig. 5 STEM image for the thick inner layer under granular NiO on the surface of the alloy 690 expose to hydrogenated SCW at 400 °C for 1000 h and corresponding selected-area diffraction patterns (SADPs)
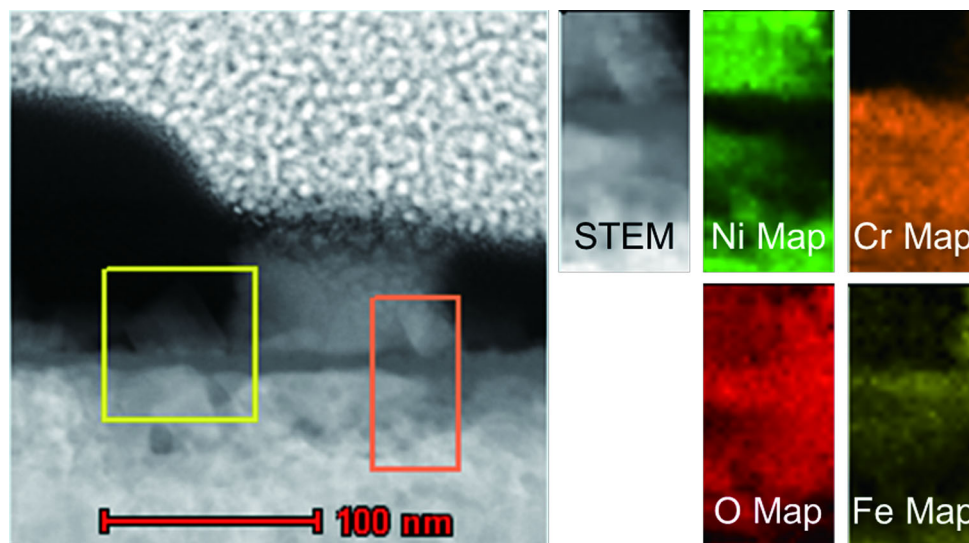

Fig. 6 EDX mapping of the oxides formed on the surface of the alloy 690 exposed to hydrogenated SCW at 400 °C for 1000 h

only composed of Ni and O, which could be NiO. Chromium concentration gradually increased in the oxide layer and became dominated in the innermost layer near the substrate. On the contrary, Ni concentration decreased across the oxide scale. In addition, iron concentration is enriched in the intermediate layer and depleted both in the
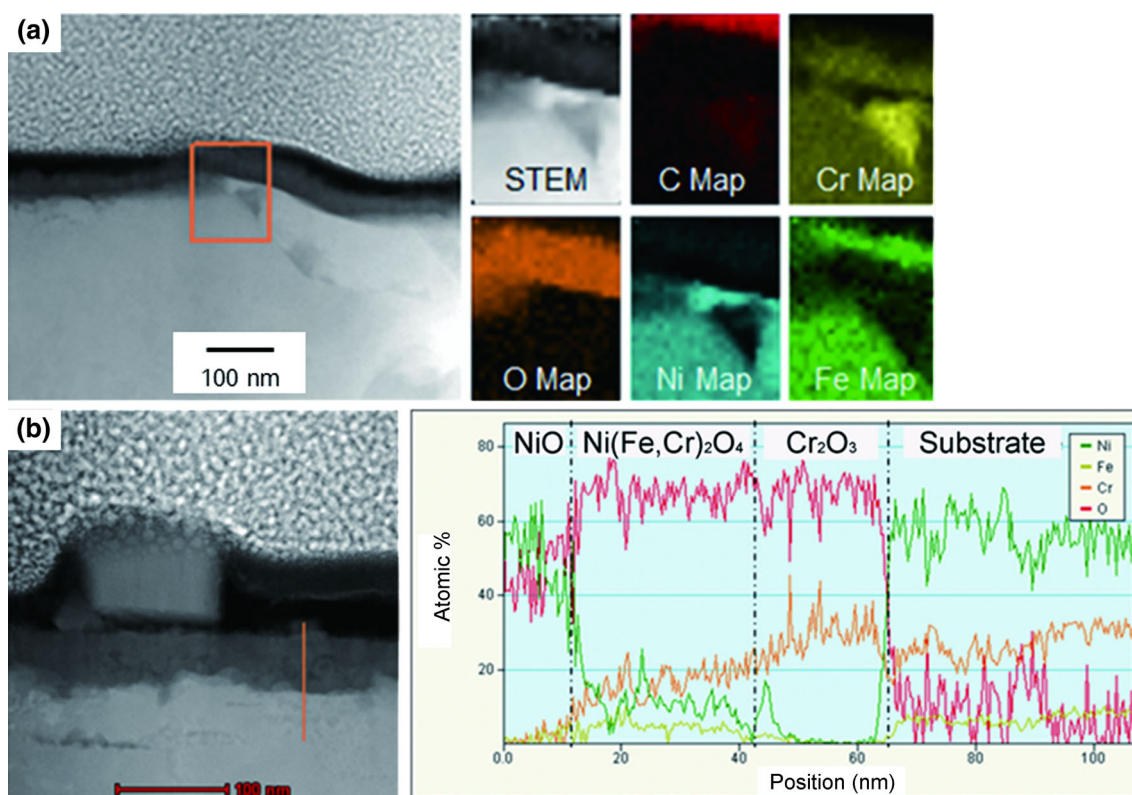
Fig. 7 STEM images and EDX mapping **a** and profile **b** spanning oxide/alloy interface on the surface of the alloy 690 exposed to hydrogenated SCW at 400 °C for 1000 h

outmost and innermost oxide layer. The profile results were in accord with the EDX mapping and cross-sectional observation in Fig. 4.

4 Discussion

The surface of the alloy 690 exposed to hydrogenated SCW at 400 °C exhibited a double-layer oxide structure: an outer layer consisted of granular crystallites and a relatively compact inner layer. The granular nickel ferrites (NiFe$_2$O$_4$) could be readily observed besides small NiO oxides. As mentioned above, the dissolved hydrogen has significant impact on the corrosion behavior of nickel alloy. In our study, the dissolved hydrogen was controlled near the Ni/NiO corrosion boundary but on the NiO stable side. Thus, the outer NiO formed. Persaud et al. [28] studied the internal oxidation of alloy 600 in hydrogenated steam, where the oxygen partial pressure was maintained below the Ni/NiO dissociation pressure. Internal oxidation was observed intragranularly with the expulsion of metallic nickel (Ni) to the surface instead of nickel oxides (NiO). For the inner layer, a monolithic Cr-rich layer formed close to the oxide/substrate interface which was supposed to be Cr$_2$O$_3$. Besides, a layer of Fe-rich oxide located between

Cr$_2$O$_3$ layer and outer NiO layer (Figs. 4, 5). An extremely similar result was reported by Zhang et al. [29]. In addition, nodules of Cr$_2$O$_3$ were observed both in the innermost oxide layer and underneath the interface in the substrate for alloy 690 (Fig. 4).

The corrosion behavior of the alloys observed in this study was in accord with the solid-state diffusion mechanism of Robertson [30]. Figure 8 presents the possible schematic mechanism of oxide formation on the surface of the alloy 690 in hydrogenated SCW. At the beginning, Ni and Cr were oxidized by the dissolved oxygen to form a mixed layer of NiO and Cr$_2$O$_3$ [31, 32] as shown in Fig. 8a. Then the oxidation could continue by outward diffusion of cations to the oxide/water interface. In nickel-base alloy, both the iron and nickel had a much higher diffusivity in oxide than chromium, so the iron and nickel would diffuse to the outer layer, while the chromium would retain in the inner layer. Cr$_2$O$_3$ particles would form a monolithic layer as shown in Fig. 8b. With the oxidation proceeding, part of NiO would transfer to stable NiCr$_2$O$_4$ spinel oxide. NiFe$_2$O$_4$ oxides could be formed by solution reaction of NiO, iron and oxygen, and then grew by the diffusion of iron. Accordingly, the size and density of NiO and large NiFe$_2$O$_4$ spinel oxides would increase with increasing duration time as shown in Fig. 8c. Concerning the alloy
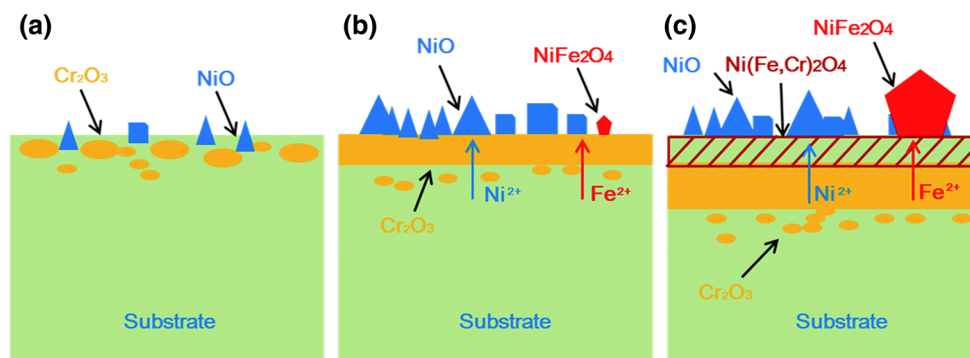
Fig. 8 Schematic mechanism of oxide formation on alloy 690 in hydrogenated SCW

under the oxide/substrate, nodules of Cr_2O_3 were observed underneath the inner oxide layer in the bulk material, distributing along the networks of defects (seemingly dislocation evidenced by STEM image in Fig. 4). It highlighted the internal diffusion of oxygen through substrate along defects, which could act as short circuits and react with chromium due to its high affinity to oxygen compared with iron and nickel. Nodules of Cr_2O_3 along the oxide/alloy interface rather than a continuous Cr_2O_3 layer on top of the substrate were also reported by other authors [33–35]. A thermodynamic classification of the oxides rated as decreasing stability was extracted in Fe–Ni–Cr–H_2O–H_2 system:

$$Cr_2O_3 > FeCr_2O_4 > NiCr_2O_4 > NiFe_2O_4 > NiO.$$

The oxide structure observed in this work was consistent with thermodynamic calculations listed above. The more stable oxides (Cr_2O_3 layer and nodules) were situated at the inner interface, whereas the less stable (NiO and $NiFe_2O_4$ crystallites) were found at the outermost interface with Cr-rich spinel oxides locating between these two layers. The inner spinel and layer of Cr_2O_3 has lower growth rate and can account for the excellent corrosion performance of alloy 690 in hydrogenated SCW. In addition, no chromium depleted zone was ever observed across the underlying alloy close to the Cr_2O_3/substrate interface, which is contrary to some previous works [31, 36, 37]. This could be explained by the different surface defect density of the samples or the different temperature used in the corrosion tests. Chromium carbides along the grain boundaries could be readily observed in nickel-based alloy 690. The presence of carbides at the grain boundaries may play a critical role in the superior property of alloy 690. Persaud et al. [28] investigated the SCC of solution annealed and thermally treated alloy 600 exposed to hydrogenated steam environment. A thicker and denser Cr-rich oxide formed at the grain boundary in thermally treated alloy 600 compared to solution annealed alloy 600, and oxygen penetration continued 700 nm inward versus 2 μm. Oxidation of Cr

carbides at the grain boundary may aid in impeding further oxygen diffusion in solution annealed alloy 600. Kuang et al. [38] ascribed the improvement of thermally treated alloy 690 over solution annealed alloy 690 in SCC resistance to the beneficial effect of the grain boundary carbides in mitigating SCC of cold rolled Alloy 690.

5 Conclusions

Oxides formed on the surface of the alloy 690 in hydrogenated SCW at 400 °C for 1000 h were studied using SEM, TEM, STEM and EDX. Preliminary results in this study showed.

1. The surface of the alloy 690 exhibited a double-layer oxide structure: an outer layer consisted of granular crystallites and a compact fine-grain inner layer.
2. Chemical analysis indicated that the outer layer was enriched in nickel but depleted in chromium, whereas the inner layer was enriched in chromium and depleted in nickel.
3. Fe-rich spinel oxides on top of a continuous Cr_2O_3 thin layer was observed in alloy 690. Besides, Cr_2O_3 nodules were readily observed in the substrate under the oxides/alloy interface.
4. The surface of the alloy 690 exhibited an oxide sequence of NiO and $NiFe_2O_4$/Ni(Fe, $Cr)_2O_4$/Cr_2O_3/alloy from the outmost oxide layer to alloy substrate.

References

[1] Y.S. Lim, H.P. Kim, S.S. Hwang, J. Nucl. Mater. **440**, 46 (2013)
[2] S.S. Hwang, H.P. Kim, J. Nucl. Mater. **440**, 129 (2013)
[3] Z. Lu, T. Shoji, S. Yamazaki, K. Ogawa, Corros. Sci. **58**, 211 (2012)

J. Gao et al.: Acta Metall. Sin. (Engl. Lett.), 2016, **29**(8), 774–781

781

[4] M. Sennour, P. Laghoutaris, C. Guerre, R. Molins, J. Nucl. Mater. **393**, 254 (2009)

[5] G. Sui, J.M. Titchmarsh, G.B. Heys, J. Congleton, Corros. Sci. **39**, 565 (1997)

[6] Q. Peng, J. Hou, K. Sakaguchi, Y. Takeda, T. Shoji, Electrochim. Acta **56**, 8375 (2011)

[7] J. Hou, Q.J. Peng, K. Sakaguchi, Y. Takeda, J. Kuniya, T. Shoji, Corros. Sci. **52**, 1098 (2010)

[8] F.H. Hua, R.B. Rebak, Environ. Crack. Mater. **2**, 141 (2008)

[9] Y. Qiu, T. Shoji, Z. Lu, Corros. Sci. **53**, 1983 (2011)

[10] T. Nakagawa, N. Totsuka, T. Terachi, N. Nakajima, J. Nucl. Sci. Technol. **40**, 39 (2003)

[11] T. Terachi, N. Totsuka, T. Yamada, T. Nakagawa, H. Deguchi, M. Horiuchi, M. Oshitani, J. Nucl. Sci. Technol. **40**, 509 (2003)

[12] S.A. Attanasio, D.S. Morton, in *11th International Conference on Environmental Degradation of Materials Nuclear Power Systems: Water Reactors* 2003, p. 143

[13] Q.J. Peng, J. Hou, T. Yonezawa, T. Shoji, Z.M. Zhang, F. Huang, E.H. Han, W. Ke, Corros. Sci. **57**, 81 (2012)

[14] F. Meng, J. Wang, E.H. Han, W. Ke, Corros. Sci. **52**, 927 (2010)

[15] Z. Zhang, J. Wang, E.H. Han, W. Ke, J. Mater. Sci. Technol. **28**, 785 (2012)

[16] D.J. Kim, H.P. Kim, S.S. Hwang, Nucl. Eng. Technol. **45**, 67 (2013)

[17] Y. Zhao, I.C. Choi, Y.J. Kim, J. Jang, J. Alloys Compd. **582**, 141 (2014)

[18] M. Casales, V.M. Salinas-Bravo, A. Martinez-Villafañe, J.G. Gonzalez-Rodriguez, Mater. Sci. Eng. A **332**, 223 (2002)

[19] P. Xu, L.Y. Zhao, K. Sridharan, T.R. Allen, J. Nucl. Mater. **422**, 143 (2012)

[20] I. Betova, M. Bojinov, V. Karastoyanov, P. Kinnunen, T. Saario, Corros. Sci. **58**, 20 (2012)

[21] W. Kuang, X. Wu, E.H. Han, Corros. Sci. **69**, 197 (2013)

[22] Z. Zhang, J. Wang, E.H. Han, W. Ke, Corros. Sci. **53**, 3623 (2011)

[23] F. Huang, J. Wang, E.H. Han, W. Ke, Corros. Sci. **76**, 52 (2013)

[24] M.J. Seo, H.S. Shim, K.M. Kim, S.I. Hong, D.H. Hur, Nucl. Eng. Des. **280**, 62 (2014)

[25] Z. Zhang, J. Wang, E.H. Han, W. Ke, J. Mater. Sci. Technol. **28**, 353 (2012)

[26] X. Zhong, E.H. Han, X. Wu, Corros. Sci. **66**, 369 (2013)

[27] W. Kuang, X. Wu, E.H. Han, J. Rao, Corros. Sci. **53**, 3853 (2011)

[28] S.Y. Persaud, A. Korinek, J. Huang, G.A. Botton, R.C. Newman, Corros. Sci. **86**, 108 (2014)

[29] Q. Zhang, R. Tang, K. Yin, X. Luo, L. Zhang, Corros. Sci. **51**, 2092 (2009)

[30] J. Robertson, Corros. Sci. **32**, 443 (1991)

[31] K.H. Chang, J.H. Huang, C.B. Yan, T.K. Yeh, F.R. Chen, J.J. Kai, Prog. Nucl. Energy **57**, 20 (2012)

[32] K.H. Chang, S.M. Chen, T.K. Yeh, J.J. Kai, Corros. Sci. **81**, 21 (2014)

[33] L. Marchetti, S. Perrin, Y. Wouters, F. Martin, M. Pijolat, Electrochim. Acta **55**, 5384 (2010)

[34] H. Lefaix-Jeuland, L. Marchetti, S. Perrin, M. Pijolat, M. Sennour, R. Molins, Corros. Sci. **53**, 3914 (2011)

[35] M. Sennour, L. Marchetti, F. Martin, S. Perrin, R. Molins, M. Pijolat, J. Nucl. Mater. **402**, 147 (2010)

[36] A. Machet, A. Galtayries, S. Zanna, L. Klein, V. Maurice, P. Jolivet, M. Foucault, P. Combrade, P. Scott, P. Marcus, Electrochim. Acta **49**, 3957 (2004)

[37] J. Panter, B. Viguier, J.M. Cloué, M. Foucault, P. Combrade, E. Andrieu, J. Nucl. Mater. **348**, 213 (2006)

[38] W. Kuang, G.S. Was, Corros. Sci. **97**, 107 (2015)